ECS The Electrochemical Society
Advancing solid state & electrochemical science & technology

On the Impact of Internal Cross-Linking and Connection Properties on the Current Distribution in Lithium-Ion Battery Modules

View the article online for updates and enhancements.

On the Impact of Internal Cross-Linking and Connection Properties on the Current Distribution in Lithium-Ion Battery Modules

Markus Schindler,[z] 🄳 Axel Durdel, 🄳 Johannes Sturm, 🄳 Philipp Jocher, 🄳 and Andreas Jossen 🄳

Institute for Electrical Energy Storage Technology (EES), Technical University of Munich (TUM), 80333 Munich, Germany

The often-observed current distribution between parallel-connected lithium-ion cells within battery modules is probably evoked by the properties of the connection, inhomogeneous contact and power line resistances, the impedance behavior of single cells and of the DoD. The extent to which each of the contributors and the interaction between them affects the current distribution within the battery module is crucial to improve the system's efficiency, which is investigated here via various electrically cross-linked, physicochemical-thermal simulations with variable system terminal (ST). Consequently, cross-connectors balance the system and reduce DoD shifts between cells. Furthermore, if one compares ST-side and ST-cross, the position of the ST is negligible for topologies that incorporate at least two cells in serial and parallel. Depending on the ST configuration, point and axis symmetry patterns appear for the current distribution. Compared to welding seam and cross-connector resistances, the string connector resistance dominates the current distribution. Like the behavior of a single cell, the system's rate capability shows a non-linear decrease with increasing C-rate under constant current discharge. As a recommendation for the assembly of battery modules using multiple lithium-ion cells, the position of the ST is of minor importance compared to the presence of cross-connectors and low-resistance string connectors.

Range anxiety is named as one of the leading reasons why people buy conventional cars instead of battery electric vehicles (BEVs).[1] At same system voltage, an increase in range can be achieved by both higher cell capacities and parallel connection of the cells. As cells with sufficient capacity still lack market maturity, parallel connection is currently the remaining alternative.[2] However, parallel connection of cells often leads to inhomogeneous current distributions. An inhomogeneous current distribution can be caused by different reasons. Thus, cell-related causes such as the cell chemistry,[2–5] deviations in resistance and capacity,[6–12] or different temperature behavior[13–16] influence the current distribution. Furthermore, the load profile[2,17] and system-related influences such as the connection properties[12,18,19] have to be taken into account. Therefore, the focus of this paper is on system-related influences and load profiles.

System-related deviations can be caused by the choice of the system terminal (ST), the internal circuit design of the serial and parallel connection of the cells, or a variation of different contact resistances. Rumpf et al.[13] investigated the influence of the ST and found that middle contacting (ST-mid) is preferable to left contacting (ST-left). Grün et al.[19] emphasized that the ratio of the cell's internal resistance to the contact resistances is particularly important. Additionally, Wang et al.[18] showed that the connector plate causes the current distribution and that their resistance therefore has to be minimized.

So far, only a few researchers have dealt with the general description of interconnected systems. Wu et al.[8] developed a semi-experimental equation system to describe serial and parallel connected cells. In contrast to Rumpf et al.[13] who described an equation system for ST-side and ST-mid, the influence of the ST on the current deviation was not taken into account. Furthermore, the possibility of inhomogeneous current distribution in parallel-connected cells was neglected by assuming that equal capacities lead to a homogeneous current distribution. For the reader's convenience, additional descriptions of interconnected systems can be found in Refs. 2, 3, 9 and 12.

Even though physicochemical models are becoming more popular due to the advantages of local analyzing opportunities,[13,14,16,20] most publications describing serial and parallel connected systems are based on equivalent circuit models (e.g. Refs. 2–4, 15, 21, 22). However, none of the existing publications describe a method of how the ST can be described flexibly or how the connection between serial and parallel strings (cross connectors) can be taken into account.

The focus of this paper is therefore on the development of a system which allows a flexible choice of the ST and considers cross-connectors. For this purpose, the model presented in our previous study[13] is developed further and the features named here are implemented. Subsequently, the influence of different STs and varying system resistances on the current distribution within a 4s4p system including cross-connectors is examined. Finally, the energy efficiency of the entire system is evaluated.

Model Structure

The electrical model (ELM) developed by Rumpf et al.[13] describes a set of X serial and Y parallel-connected cells and is the basis for the extension presented in this paper. Therefore, the components and the nomenclature of the ELM as well as the coupled simulation model are briefly described. Following that, the extensions of the ELM and the calculation method of the cell currents are discussed. The last part of this section addresses the assumptions made for the simulation.

Basics of the electrical model.—The ELM of a 4s4p system including cross-connectors is illustrated in Fig. 1. Additionally, Table I lists all components of the ELM with a short description. Based on their numbering, the components of Fig. 1 can be clearly assigned. As Fig. 1 illustrates, the numbering of the cells corresponds to the numbering of matrix elements. Therefore, the numbering of the cells c starts at the top left with $c_{1,1}$ and ends at the bottom right with $c_{X,Y}$. Both the numbering of the cell currents I and the resistances of the welding seams on the positive (R_{wsp}) and negative (R_{wsn}) tabs of the cell equal the cell numbering. The connector resistance between two serial cells R_{conn} gets its number from the cell above it. R_p and R_n are the string connector resistances on the top and bottom between two parallel strings and are therefore numbered according to the string number to their right. The numbering of these string connector resistances ends by Y. If one

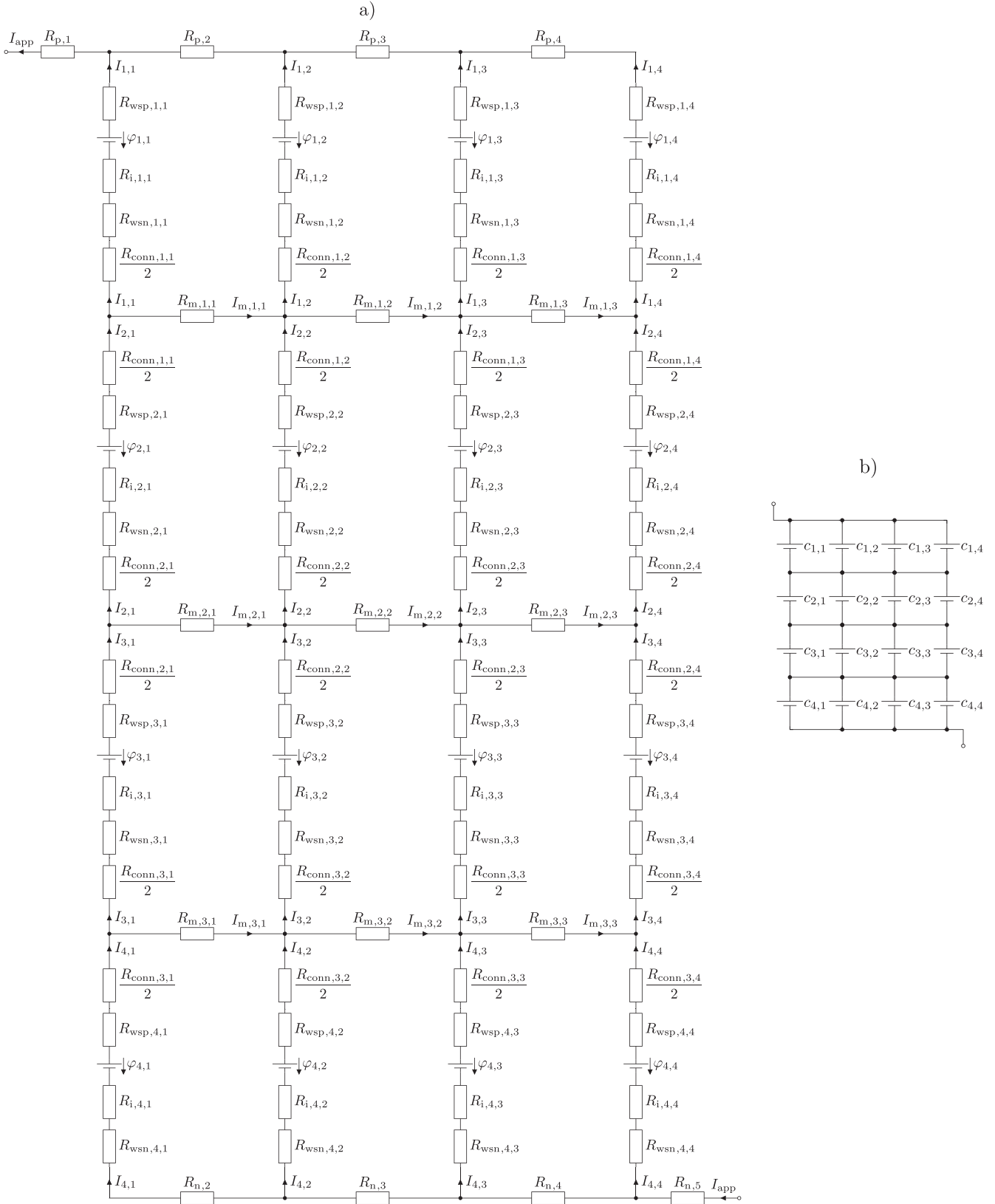[z]E-mail: markus.ms.schindler@tum.de

Figure 1. System topology of the ELM for a 4s4p system. Part (a) shows the entire system, including all of its components. Part (b) is the graphically reduced version and will be used instead of (a) in the following. For both versions, the STs are positioned in a cross wise manner. Cross-connectors between adjacent strings and cells resemble a connector plate.

of the STs is positioned on the right side, the numbering ends by $Y + 1$. Note that there is no R_{conn} present at the link between R_{wsp} and R_p. This is due to the assumption that the tabs are directly welded onto the busbar leading to the ST (see Eq. 6). The same applies to R_{wsn} and R_n, respectively. The numbering of the cross-connector resistances R_m between two serial-connected cells and two

Table I. Descriptions, units, and initial values of the components used in the ELM.

Variable	Initial Value	Unit	Description
ϕ	4.2	V	Voltage of a single cell
I	1 C	A	Current through single cell
I_{app}	$Y \cdot 1$ C	A	Current applied to the system
I_{m}	0	A	Current through cross-connector m
R_{i}	28.7	mΩ	Internal resistance of a single cell
R_{wsp}	62.5	$\mu\Omega$	Resistance of the welding seam at the positive tab
R_{wsn}	62.5	$\mu\Omega$	Resistance of the welding seam at the negative tab
R_{conn}	30.9	$\mu\Omega$	Resistance of the serial connection within a string
R_{m}	15.4	$\mu\Omega$	Resistance of the cross-connector between two strings
R_{p}	15.4	$\mu\Omega$	Resistance of the parallel connection at the positive tab
R_{n}	15.4	$\mu\Omega$	Resistance of the parallel connection at the negative tab

parallel strings is separated from the cell numbering, but also corresponds to the numbering of matrix elements.

In order to clarify the naming of the system, in addition to the number of cells connected in serial and in parallel, the location of the ST (left or cross) is also added. Fig. 1 illustrates the system for ST-cross. Furthermore, the system includes four cell packages (I–IV). One cell package includes all cells at the same level of serial connection. For example, cell package III includes the cells $c_{3,1}$, $c_{3,2}$, $c_{3,3}$, and $c_{3,4}$.

Extension of the electrical model.—As shown in Fig. 2, Rumpf et al.[13] coupled the ELM with a physicochemical model (PCM) and a thermal model (THM). The coupled model was then used to investigate the influence of the ST, the contact resistance and varying internal resistances, capacities and temperature gradients on the current distribution within parallel-connected lithium iron phosphate (LFP) cells. To calculate the string currents, Kirchhoff's nodal and mesh equations were used and an equation system was given.

However, calculating systems including cross-connectors (see Fig. 1) is not possible with the developed equation system. Additionally, the position of the ST is limited to a side (left or right) and middle connection. Hence, two extensions of the ELM are necessary. First, the model should be capable of dealing with systems including cross-connectors, and second, the position of the ST should be freely chosen.

To ensure that the ST can be freely chosen, setting up the meshes to calculate the string currents has to be considered. Therefore, attention has to be paid to the node where the currents branch differently. Consequently, the sign of affected R_{n} and R_{p} has to be adjusted if necessary. The sign of all other components as well as the general calculation method for the currents remains the same as described by Rumpf et al.[13]

However, including cross-connectors in the ELM has more impact on the calculation algorithm because the mesh equations have to be defined differently. In addition to the increased number of cell currents I, the currents I_{m} through the cross-connector resistances have to be calculated as well. This means that every additional cross-connector adds three additional variables to the equation system. Note that cross-connectors can only be implemented when $X, Y \geqslant 2$ holds true. To achieve at least a quadratic equation system, the same number of equations has to be added. Therefore, the procedure of adding equations is explained for a 2s2p system (ST-left), shown in Fig. 3.

In Fig. 3a, only two currents have to be calculated, since the currents through $c_{1,1}$ and $c_{2,1}$ as well as through $c_{1,2}$ and $c_{2,2}$ are equal. Therefore, two equations are generated by the node k_1 on the bottom of string 1 and the mesh m_1 in between the cells. This leads to a quadratic equation system that can be solved analytically.

By including the cross-connector in Fig. 3b, three additional currents are generated. Now, the four cell currents $I_{1,1}$, $I_{1,2}$, $I_{2,1}$, and
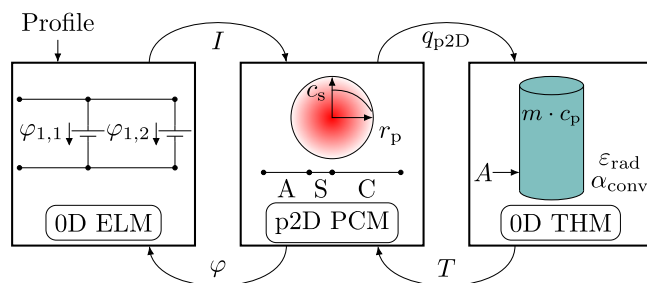
Figure 2. Coupling of the PCM, ELM, and THM according to Rumpf et al.[13] An electrical load is applied to the ELM in form of a profile. The shown exchange variables are used to couple the three models.
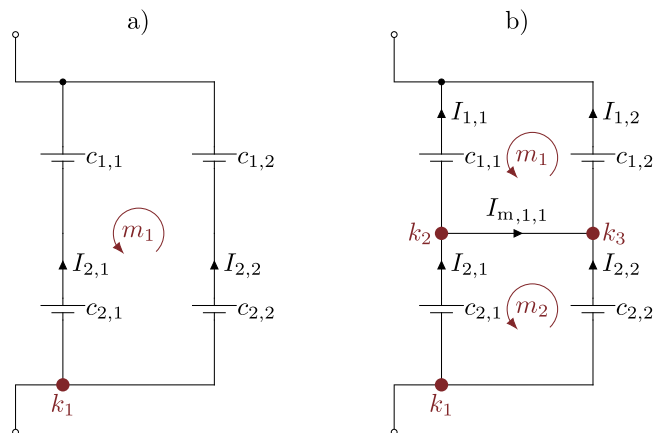
Figure 3. A 2s2p system (a) without and (b) including a cross-connector, highlighting the impact of the cross-connector on the number of currents/equations necessary. In part (a), only two currents are needed to describe the system. In part (b), however, five currents can be distinguished.

$I_{2,2}$ as well as the current $I_{\text{m},1,1}$ through the cross-connector have to be calculated. To do so, the meshes m_1 and m_2 between $c_{1,1}$ and $c_{1,2}$ as well as between $c_{2,1}$ and $c_{2,2}$ are determined. Additionally, the node k_1 on the bottom of string 1 and the nodes k_2 and k_3 at the connection points on the left and right of the cross-connector are considered. Consequently, three additional equations are generated and the equation system is analytically solvable. If the system is extended by another cell package in serial or string in parallel, additional resulting nodes and meshes surrounding the additional cross-connectors have to be defined to retrieve the required equations. Consequently, it can be summarized that even in a system including cross-connectors, enough equations can be determined to set up a quadratic equation system.

Specifications of the simulation scenarios.—The PCM and THM used in this study are based on the model developed by Sturm et al.[23,24] The model development and its parametrization for a nickel-rich manganese cobalt (NMC-811), silicon-graphite (SiC) lithium-ion cell (LG Chem, INR18650-MJ1, 3.35 Ah[25]), using a wide range of experimental measurements, are shown in detail in Refs. 23, 24. The model equations and the resulting parametrization are summarized in Tables A·I and A·II as well as in Fig. A·1. To maintain the validity of the single cell model the presented simulation studies were chosen within the experimental validated operating range. The single cell PCM shows a mean open-circuit-voltage (OCV) error of 5.7 mV and a mean error of 13.5 mV for 1 C discharge (see Ref. 23, Figs. 1b and 4f). The THM shows a mean temperature error of less than 0.1 K (see Ref. 24, Fig. 4d)) for the intended C-rates. Therefore, it is assumed that the PCM and THM do not significantly affect the results. Furthermore, the following assumptions were made: It is assumed that the subsequently calculated resistances apply to industrially produced, interconnected systems using large format cells. Currently, such systems can be found mainly in BEVs. The available Audi, Jaguar, and Porsche BEVs can be seen as examples.[26–28] Additionally, each cell of the system is assumed to have the same capacity, internal resistance, and thermal behavior. Unless stated otherwise, the initial values correspond to those of Table I and the ambient temperature is set to 25 °C. Moreover, the tabs of the cells are considered to be welded onto an aluminum connector plate with a thickness of 2 mm using two 14 mm welding seams on each tab.

Schmidt et al.[29] measured a contact resistance of $R_{Al-Al} = 250~\mu\Omega$ for Al–Al connections built on a single welding seam with an area of 15.71 mm^2. Due to the doubled welding seams, the contact resistance decreases by a factor of 2. Moreover, it is assumed that due to industrialized welding techniques and increased welding areas, the contact resistance can be decreased by an additional factor of 2. In total, the contact resistance of R_{wsp} and R_{wsn} is set to 62.5 $\mu\Omega$. Furthermore, the average distance between the positive and negative tabs l_{ws} of the cells connected in serial is assumed to be 3 cm. Additionally, the average distance of adjacent positive or negative tabs is set to be $0.5 \cdot l_{ws}$. With an electrical conductivity of aluminum of $\sigma_{Al} = 34.7 \cdot 10^6$ S m^{-1},[29] the values of R_{conn} and R_m can be calculated using Eqs. 1 and 2. R_n and R_p are assumed to have the same characteristics as R_m and are therefore set to the same value (Eq. 3).

$$
\begin{aligned}
R_{conn} &= \frac{1}{\sigma_{Al}} \cdot \frac{l_{conn}}{l_{ws} \cdot t_{conn}} \\
&= \frac{1}{34.7 \cdot 10^6~\text{S m}^{-1}} \cdot \frac{0.03~\text{m}}{0.014~\text{m} \cdot 0.002~\text{m}} = 30.88~\mu\Omega
\end{aligned}
$$
[1]

$$
\begin{aligned}
R_m &= \frac{1}{\sigma_{Al}} \cdot \frac{W_m}{h_m \cdot t_m} \\
&= \frac{1}{34.7 \cdot 10^6~\text{S m}^{-1}} \cdot \frac{0.015~\text{m}}{0.014~\text{m} \cdot 0.002~\text{m}} = 15.44~\mu\Omega
\end{aligned}
$$
[2]

$$
R_n = R_p = R_m
$$
[3]

A common feature of the BEVs mentioned here is the use of large format lithium-ion batteries with a capacity of approx. 60 Ah. In order to ensure practical relevance, a capacity of 60 Ah is therefore assumed to be the reference cell capacity in the following. However, the model developed by Sturm et al.[23] was validated for a 3.35 Ah cell. As the cell under consideration and the cell used by Sturm et al.[23] differ in capacity and resistance, the values of R_{wsp}, R_{wsn}, R_{conn}, R_m, R_p, and R_n from Table I have to be scaled to ensure comparability. Therefore, a scaling factor scaling factor *SF* has to be calculated, using the ratios of the cells' capacities or internal

Table II. Overview of the investigated cases.

Investigation	Initial Value	Variation
ST	—	left, cross
R_{wsp}	62.5 $\mu\Omega$	+100%
R_m	15.4 $\mu\Omega$	+100%
R_p	15.4 $\mu\Omega$	+100%
I_{app}	1 C per cell	C-rate

resistances. Since the focus of this study is not on high power but on high energy applications, the influence of the capacity should dominate the influence of the resistances. Consequently, the initial values of the resistances named here are scaled by the cells' capacities using $SF_C = 17.9$.

Subsequently, the influence of different STs, varying R_{wsp}, R_m, and R_p on the current distribution is discussed. Therefore, a side (ST-left) and cross-connection (ST-cross) are investigated first. Following this, the influence of varying R_{wsp} are examined. The value of the homogeneous case is therefore increased by +100%. Next, the same variation is applied to different R_m. Finally, the rate capability of the extractable energy content of the system is examined. Note that only one R_{wsp}, R_m, or R_p is varied at a time. Table II summarizes the investigated cases. Note that Rumpf et al.[13] showed that middle contacting would lead to a more homogeneous current distribution. Consequently, the deviations shown in the following exceed the deviations of middle contacting, which is why the focus of the following investigations is on ST-left and ST-cross.

As described above, it is assumed that every cell has the same thermal behavior. Consequently, the conditions (see Tables A·I and A·II) applied to the cells are equal. Furthermore, thermal coupling between adjacent cells as well as heat transfer through contact surfaces have not yet been implemented in the THM. Therefore, an equal current load leads to an equal temperature behavior, independently of a cell's position within the system. As shown below, the current distribution throughout the system exhibits relatively small deviations between cells over a wide depth of discharge (DoD) range. Consequently, uneven temperature development is not expected to have a significant influence on the current deviation for the investigated cases. However, the development of a thermally coupled model and the analysis of temperature gradients and cooling strategies within battery systems are crucial for cooling strategies and battery safety and may be the scope of future studies.

The applied current to the system equals $Y \cdot I_{1C}$. That in turn means that the expected current load per cell is equal to a C-rate of $I = 1$ C (I_{1C}). Each discharge begins with fully charged cells (DoD = 0) at a cell voltage of 4.2 V and ends when a cell reaches the discharge cutoff voltage of 2.5 V (DoD = 1). This means that for the investigated 4s4p system the measurable voltage level at the STs is between 16.8 V and 10.0 V. Furthermore, the expected amount of energy that can be drawn from the system equals the sum of the extractable energies of the individual cells and can be calculated using the following equation:

$$
E_{sys} = \sum_{s=1}^{X} \sum_{p=1}^{Y} E_{s,p}
$$
[4]

In this matter, the nominal energy ($E_{N,sys}$) is summarized from the total of all cells ($16 \cdot E_{N,cell}$), which is used to compare the simulated cases shown in Table II.

Results

The following results are based on the systems 4s4p ST-left and 4s4p ST-cross, as described above. Both systems include cross-connectors.

Influence of the system terminal.—Figure 4 illustrates the resulting current distribution of a 4s4p system connected on the
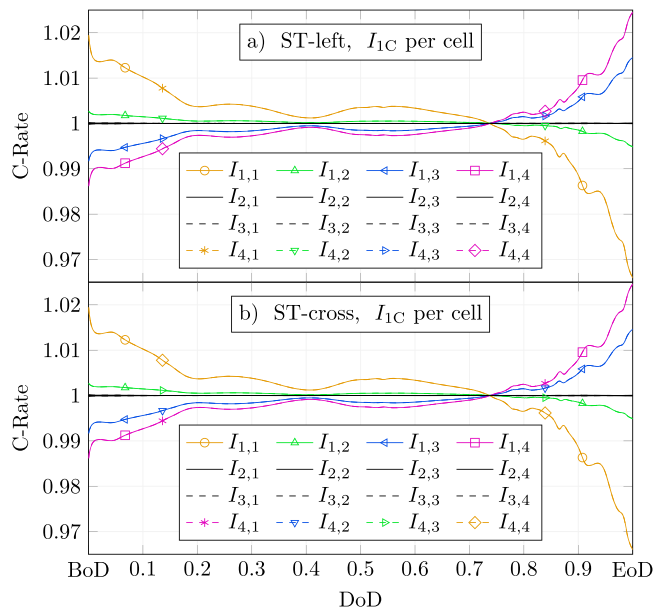
Figure 4. Influence of the STs on the current distribution in the homogeneous case for a 4s4p system including cross-connectors. The system in (a) is contacted on its left side (ST-left), the system in (b) is cross-connected (ST-cross).
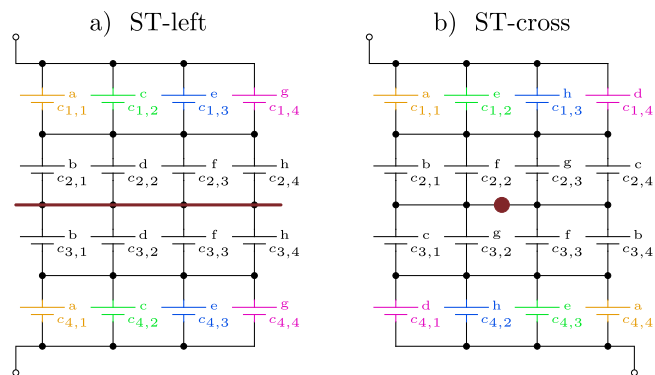

Figure 5. Resulting symmetry for homogeneous interconnected systems. Side connection (a) leads to axis symmetry, cross-connection (b) leads to point symmetry. As in Fig. 1, the numbers stand for the cell index. Colors and letters both highlight the symmetry and thus mark symmetry partners.

left side (ST-left, (a)) and cross-connected (ST-cross, (b)), for the homogeneous case. Homogeneous here means that the same system components have the same initial values. By comparing Figs. 4a and 4b qualitatively, it can be seen that there is no difference between the current distribution within the systems. Note that equal line colors indicate quasi-identical current distributions of different cells within the systems. Therefore, it can be stated that within $XsYp$ systems including cross-connectors, the choice of the ST is negligible for the homogeneous case, if $X, Y \geqslant 2$ holds true.

Additionally, five current paths can be distinguished in both subplots. As a total of 16 current distributions have to occur for the analyzed 4s4p system, the noticeable current paths can be interpreted as group current paths. It is therefore necessary to clarify where the number of group paths originates from and how the groups are formed.

Considering Fig. 4, the number of group paths strongly depends on the number of cells connected in parallel, since a group current path occurs for each of the Y parallel strings. These current paths differ from the applied current of I_{1C} for the first and the last cell package of the system due to uneven path resistances R_{PR}.[2,13] For parallel-connected systems with $X > 2$, an additional group current path occurs which lies directly on the applied current line.

Consequently, the number of group current paths N_{GCP} within a $XsYp$ system is given by the following rule:

$$N_{GCP} = \begin{cases} Y & \text{for } X \leqslant 2 \ \wedge \ Y \geqslant 2 \\ Y + 1 & \text{for } X > 2 \ \wedge \ Y \geqslant 2 \end{cases} \quad [5]$$

Marking the cells from the same group current path in Fig. 1b leads to Fig. 5. Considering ST-left shown in Fig. 5a, the current distribution within the system follows the axis symmetry to the mirror axis between cell packages II and III. On the other hand, the current distribution regarding ST-cross leads to point symmetry to the central point of the system of Fig. 5b. Once again, the symmetries can be justified with the cells' R_{PR}. For example in the case of ST-cross R_{PR} of $c_{1,3}$ and $c_{4,2}$ to the nearest ST calculate to:

$$R_{PR,1,3} = \frac{R_{conn,1,3}}{2} + R_{wsp,1,3} + R_{i,1,3} \\ + R_{wsn,1,3} + R_{p,3} + R_{p,2} \quad [6]$$

$$R_{PR,4,2} = \frac{R_{conn,3,2}}{2} + R_{wsp,4,2} + R_{i,4,2} \\ + R_{wsn,4,2} + R_{n,3} + R_{n,4} \quad [7]$$

Since Eqs. 6 and 7 consist of equal system elements with equal values, the same current is applied to $c_{1,3}$ and $c_{4,2}$.

The symmetry effects found can now be used to examine the maximum deviations from the applied current at the beginning of discharge (BoD) and at the end of discharge (EoD) (see Fig. 4). Note that the choice made for BoD and EoD represents the maximum deviation during the entire discharge of the cells, as can be seen in Fig. 4. This is why the deviations from the applied current at these points in time can be assumed to be a worst-case scenario. Table III lists the deviations from the applied I_{1C} discharge current for cells $c_{1,1}$, $c_{1,2}$, $c_{1,3}$ and $c_{1,4}$ for the homogeneous case.

Thus, at the beginning, $I_{1,1}$ and $I_{1,2}$ are increased by 1.9% and 0.3% due to their smaller R_{PR} as compared to the applied I_{1C} current. In contrast, $I_{1,3}$ and $I_{1,4}$ are decreased by 0.8% and 1.4%. Consequently, until currents cross at around 75% DoD, $c_{1,1}$ and $c_{1,2}$ are discharged with a higher current and their DoD increases faster. Subsequently, $c_{1,3}$ and $c_{1,4}$ have to compensate for this imbalance until the EoD. Therefore, $I_{1,3}$ and $I_{1,4}$ increase up to 1.5% and 2.4% compared to the applied I_{1C} current. Depending on the choice of the ST, these deviations correspond to the deviations of the symmetry partners marked in Fig. 5. Cells of cell packages II and III are not listed because their maximum deviation to the applied I_{1C} current is less than 0.02% and is therefore considered negligible. Furthermore, an extractable energy content for the homogeneous case E_{hom} of 193.2 Wh occurs for both systems. Since the nominal energy content of a single cell calculates to $E_{N,cell} = 12.18$ Wh, following Eq. 4 $E_{N,sys}$ calculates to 194.9 Wh. Consequently, 99.13% of $E_{N,sys}$ can be extracted for the homogeneous case.

The analysis by Hofmann et al.,[3] performed with an equivalent circuit model using linearized OCV, showed that differences in OCV, impedance, and capacity are the main reasons for an inhomogeneous current distribution within parallel connections. Thereby, differences in the OCV dominate the influences of uneven capacity and impedance.

Table III. Maximum deviation to the applied I_{1C} current at the beginning (BoD) and at the end of discharge (EoD). The same deviations apply to the symmetry partners of the cells according to Fig. 5.

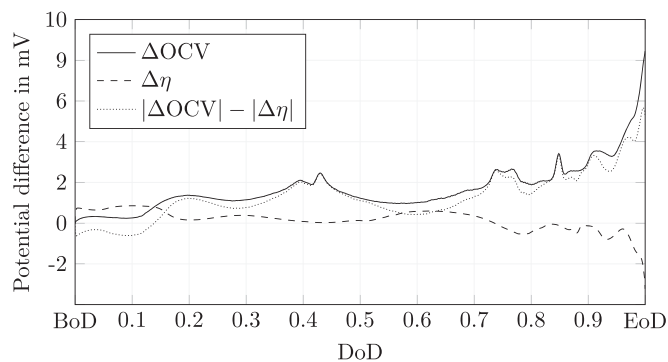|	$\Delta I_{1,1}$	$\Delta I_{1,2}$	$\Delta I_{1,3}$	$\Delta I_{1,4}$
BoD	+1.9%	+0.3%	−0.8%	−1.4%
EoD	−3.4%	−0.5%	+1.5%	+2.4%

Figure 6. Analysis of the differences in polarization and OCV for cells $c_{1,1}$ and $c_{1,2}$ of the homogeneous 2s2p system of Fig. 3b for a 1 C discharge. The difference Δ indicates the difference between cell $c_{1,2}$ and $c_{1,1}$, i.e. $OCV_{1,2} - OCV_{1,1}$. Differences in the polarization at surrounding components are not included in the diagram.
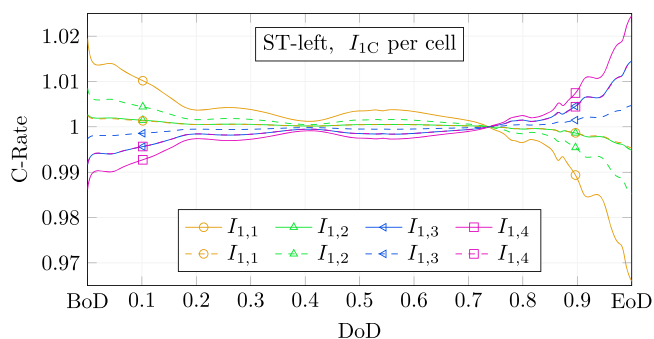

Figure 7. Influence of the variation of $R_{wsp,1,1}$ (dashed lines) on the current distribution within cell package I as compared to the homogeneous case (solid lines).

To further analyze the origin of the current distribution, the PCM was used to perform a polarization analysis.[30] With respect to the complexity, the analysis was conducted for the upper cell package in Fig. 3b instead of a cell package of the 4s4p system. The parametrization of the PCM, ELM, and THM remained unchanged (see Table II). Figure 6 illustrates the resulting differences in polarization and OCV between the cells. Since $R_{PR,1,1}$ is decreased as compared to $R_{PR,1,2}$, $c_{1,1}$ is discharged with an increased current compared to $c_{1,2}$ at the BoD. Since the polarization of the single cell depends on the current, the resulting inhomogeneous current distribution causes a difference in the polarization of $c_{1,1}$ and $c_{1,2}$. In addition, as both cells are discharged from 0% DoD, no OCV shift occurs at the BoD. Hence, the current distribution is caused by the differences in R_{PR} and polarization during the BoD. However, with progressive discharge of the cells, the inhomogeneous current distribution leads to a difference of the cells' DoDs. As a result, the cells' OCVs are shifted against each other. Figure 6 also illustrates that as soon as the difference of the OCVs exceeds the difference of the polarizations, the shift of the cells' OCVs becomes dominant. As the OCV difference leads to different cell potentials, the current distribution is dominated by the OCV difference. For the modeling design, this means that the use of a validated equivalent circuit model could also be justified. However, since the polarization analysis is seen as an important tool for subsequent studies, a PCM model was also used for the sensitivity analysis shown in the following. Note that Fig. 6 does not include differences of the polarization at surrounding components, and thus the difference between the cells' OCVs and the internal polarizations η differs from zero.

Influence of the welding seam resistance.—The influence of R_{wsp} on the current deviation within both systems is analyzed next. For this purpose, all R_{wsp} are successively increased by +100% for ST-left and ST-cross.
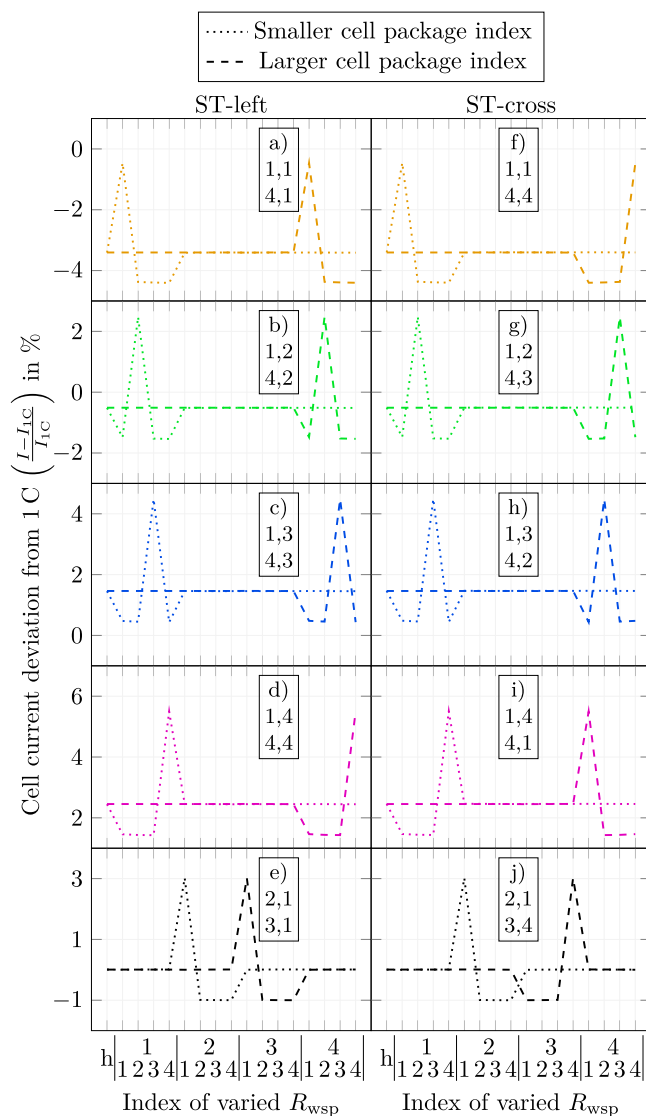

Figure 8. Influence of varying R_{wsp} on the current distribution within interconnected 4s4p systems. Each subplot illustrates the current deviation from I_{1C} for the symmetry partners of the cell package with the smaller (dotted) and larger (dashed) index at the EoD. The x-axis refers to the varied (+100%) R_{wsp}, whereas h represents the homogenous case. Consequently, the influence of the varied R_{wsp} on the cell of interest can be seen in the related subplot.

Figure 7 illustrates an example of the resulting current profile of the 4s4p system (ST-left) for a variation of $R_{wsp,1,1}$ as compared to the homogeneous case. Due to the increased contact resistance of $c_{1,1}$, $I_{1,1}$ decreases in the beginning. At the same time, $I_{1,2}$, $I_{1,3}$, and $I_{1,4}$ have to increase so that cell package I can still pass on the required current to the next cell package level (II). Consequently, the increased current through cells $c_{1,2}$, $c_{1,3}$, and $c_{1,4}$ at the BoD leads to a faster discharge of these cells. This in turn means that at the EoD, $c_{1,1}$ has to deliver a higher current as compared to the homogeneous case, whereas the currents through $c_{1,2}$, $c_{1,3}$, and $c_{1,4}$ decrease. This means that there is always an interplay of the current load within the cell package so that the overall applied current of $4 \cdot I_{1C}$ can be passed on to the next cell package. Hence it is examined next, if a variation of R_{wsp} only affects cells within the same cell package and therefore, whether every cell package can be analyzed independently.

Accordingly, Fig. 8 illustrates the deviations of the cell currents at the EoD (see Fig. 7) as compared to the applied I_{1C} current for a variation of R_{wsp}. On the left side of Fig. 8, every subplot illustrates the influence of R_{wsp} on the current deviation of the symmetry
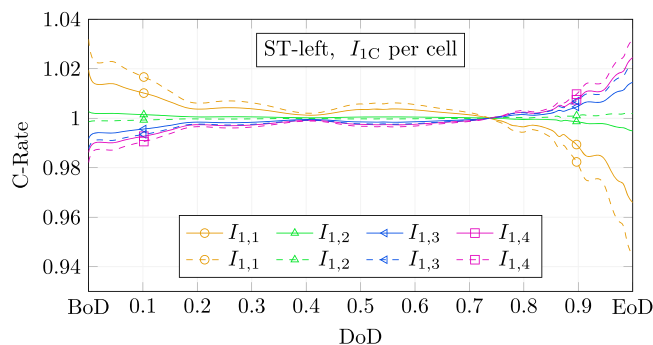
Figure 9. Influence of the variation of $R_{p,2}$ (dashed lines) on the current distribution within cell package I as compared to the homogeneous case (solid lines). The result is independent of the ST.

partners for ST-left. Consequently, the influence of $R_{wsp,1,1}$ on the currents of cell package I can be investigated by comparing the deviation of $I_{1,1}$, $I_{1,2}$, $I_{1,3}$, and $I_{1,4}$ in the subplots (a), (b), (c), and (d) (dotted lines) above index 1,1. In contrast, if a variation of $R_{wsp,1,1}$ would affect cell currents of cell packages II, III, or IV, at least one cell current of $I_{2,1}$, $I_{3,1}$, $I_{4,1}$, $I_{4,2}$, $I_{4,3}$, or $I_{4,4}$ would deviate from the homogeneous case (index h) under variation of $R_{wsp,1,1}$ (index 1,1) in Fig. 8. As this is not the case, it can be stated that a variation of $R_{wsp,1,1}$ only affects cell currents within cell package I. If one continues to analyze the effects of the variations in other R_{wsp} (index $1,2 - 4,4$), this statement by cell package I can be extended to the entire system. Accordingly, it can generally be stated that an increased contact resistance only affects the cell package in which the increased contact resistance occurs. Thus, each cell package can be evaluated in a decoupled manner. The reason why a variation within a cell package has no influence on the surrounding cell packages is the presence of cross-connectors between the cell packages. Consequently, cross-connectors can be seen as balancing elements inside the system.

Due to the finding that cell packages can be analyzed individually, the position of an increased R_{wsp} within the cell package is investigated further. Hence, a variation of $R_{wsp,1,1}$, $R_{wsp,1,2}$, $R_{wsp,1,3}$, or $R_{wsp,1,4}$ leads to a maximum increase at the EoD of the currents $I_{1,1}$, $I_{1,2}$, $I_{1,3}$ or $I_{1,4}$, of 2.94%, 2.98%, 3.01%, or 3.04% as compared to the homogeneous case. Referring to the symmetry partners shown in Fig. 5, the same deviations occur for a variation of R_{wsp} within cell package IV. Within cell packages II and III, a deviation of 3.01% as compared to the homogeneous case remains the same for every varied R_{wsp}, as indicated by the subplots (e) and (j) in Fig. 8. The maximum difference between the deviations of all investigated cases can be calculated to 0.1%. Consequently, the influence of the position of an increased R_{wsp} has no significant impact on the rate of current increase for the analyzed system. The reason for this is that the ratio between R_{wsp} to the resistance of R_m and R_p is dominated by the welding seam resistances. An increase of R_{wsp} reinforces this effect, which is why the named resistances are even less important.

Additionally, the impact of R_n, R_p, R_m, and R_{conn} on the maximum cell current load can be examined by evaluating the deviation at the EoD as compared to the applied I_{1C} current rate. Thus, $I_{1,1}$, $I_{1,2}$, $I_{1,3}$, and $I_{1,4}$ deviate at the EoD from the applied I_{1C} current in the homogeneous case by -3.41%, -0.51%, 1.46%, and 2.45%, and under variation of the corresponding R_{wsp} by -0.46%, 2.48%, 4.48%, and 5.50% (see Fig. 8). Therefore, it can be determined that in both cases, the maximum cell current load increases with increasing distance to the ST for cell package I. This can in turn be explained by the fact that an increased distance from the ST corresponds to an increased R_{PR}, which leads to a lower current load during the BoD and an increased current load during the EoD (see also Fig. 7). As described above, an increase of R_{wsp} reinforces this effect. Therefore, it can be summarized that the position of an increased R_{wsp} has no impact on the rate of current increase within the cell package, but on the maximum current deviation at the EoD.

Varying R_{wsp} within a 4s4p ST-cross system leads to the results in Figs. 8f–8j. Compared to the results of ST-left, only the symmetry partners change according to Fig. 5b for ST-cross. The aforementioned conclusions apply similarly for the cross-connected system. That also holds true for the influence of the position and the rate of current increase that corresponds to the variation of R_{wsp}.

Furthermore, only a negligible influence of a variation of R_{wsp} on the extractable energy content can be observed, as the difference between the maximum and the minimum extractable energy only calculates to 0.01 Wh. This in turn means that an increased R_{wsp} by $+100\%$ could not be detected by the measurable extractable energy content at the system terminals.

Influence of the cross-connector resistance.—In addition to the influence of R_{wsp}, the influence of increased R_m on the current distribution is investigated next. For this reason, R_m were increased individually by $+100\%$ for both system configurations. Table IV evaluates the maximum current deviation of I_m as compared to the homogeneous case under variation of R_m. Therefore, it can be seen that $R_{m,1,2}$ and $R_{m,3,2}$ show the highest current deviation of $\Delta I_{max} = 0.024\%$. This current is distributed to the subsequent cell package differently than in the homogeneous case. Moreover, in the worst case, ΔI_{max} is passed on to only a single cell of the next cell package over the entire I_{1C} discharge. Compared to I_{1C}, an additional deviation of ΔI_{max} corresponds to a current of 0.024% of the cells' current. Such a deviation is therefore classified as not significant. Furthermore, the extractable energy content under a variation of R_m equals the value of the homogeneous case. Accordingly, it can be said that an increase of R_m by $+100\%$ has no significant influence on either the current distribution or the extractable energy content of the analyzed system.

Taking into account the respective symmetry partner, Table IV and the statements made apply equivalently to ST-cross.

Influence of the string connector resistance.—After investigating the influence of R_{wsp} and R_m, the influence of varying string connectors is examined next. Therefore, $R_{p,2}$, $R_{p,3}$, and $R_{p,4}$ of cell package I are successively increased by $+100\%$ for both systems. A variation of $R_{n,2}$, $R_{n,3}$, and $R_{n,4}$ is omitted, due to symmetry effects to cell package I.

Figure 9 illustrates the current distribution within cell package I for a variation of $R_{p,2}$ in a system with ST-left. Compared to the homogeneous case, $I_{1,1}$ is increased by 1.3% at the BoD whereas $I_{1,2}$, $I_{1,3}$, and $I_{1,4}$ are decreased by 0.5%, 0.4% and 0.4%. The reason for this deviation is that the string connectors can be seen as segmenting elements of the system. The segmenting in turn leads to increased R_{PR} for all strings, whose position in the current path is behind the varied resistance. Consequently, strings with higher R_{PR} lead to lower string currents at the BoD, and thus $I_{1,2}$, $I_{1,3}$, and $I_{1,4}$ are decreased during the BoD and only $I_{1,1}$ is increased. Consequently, if $R_{p,2}$ is increased, cell package I divides into two segments. String 1 is located in front of the increased string connector and experiences a higher current during the BoD because of the lower path resistance. However, if $R_{p,3}$ is varied, the deviation of $I_{1,1}$ and $I_{1,2}$ is smaller, since the additional current can split up to both strings. In contrast to $R_{p,2}$ and $R_{p,3}$, $R_{p,4}$ takes a special place, as it is the last string connector. Figure 1 illustrates that $R_{p,4}$ acts as an element of the string itself rather than as a string connector. Thus, a variation of $R_{p,4}$ leads to the same findings as varying $R_{wsp,1,4}$.

Comparing the maximum current deviations occurring for a variation of R_{wsp} (see Fig. 8) to those of a variation of R_p, the influence of varying R_{wsp} seems to dominate R_p's influence. However, taking into

Table IV. Maximum current deviation of I_m as compared to the homogeneous case under variation of R_m by $+100\%$. The entries marked with * have a maximum deviation of less than $3 \cdot 10^{-6}\%$ and were therefore set to zero.

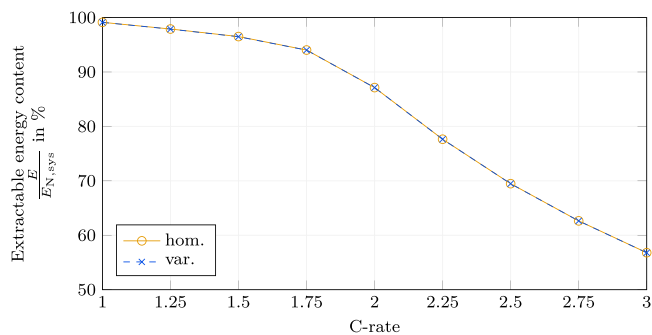|					
$R_{m,1,1}$	0.016%	$R_{m,1,2}$	0.024%	$R_{m,1,3}$	0.011%
$R_{m,2,1}$	0%*	$R_{m,2,2}$	0%*	$R_{m,2,3}$	0%*
$R_{m,3,1}$	0.016%	$R_{m,3,2}$	0.024%	$R_{m,3,3}$	0.011%

Figure 10. Extractable energy content of the analyzed 4s4p system for different C-rates. Solid lines show the amount in the homogeneous case, dashed lines refer to an increase of $R_{p,2}$ by +100%.

account that there is a factor of 4 between the increased values of R_p and R_{wsp} and only a factor of 1.7 between the maximum deviations at the EoD, it can be determined that the influence of R_p dominates the influence of R_{wsp} on the current distribution within the system. The same applies for R_m, since, as shown above, the influence of a variation of R_m is negligible. Consequently, it can be stated that attention has to be paid to the string connectors when assembling such a system.

The maximum deviation of the extractable energy from the homogeneous case calculates to 0.02 Wh for a variation of R_p. Thus, even an increased string connector resistance cannot be detected by means of the measurable extractable energy content. This in turn means that none of the investigated cases can be detected due to measurable quantities at the STs. The almost constant extractable energy is thus achieved by a higher load on individual system components (see deviations in Fig. 9). The impact of this effect on the durability of the components and thus of the investigated system therefore needs to be investigated in further studies.

Rate capability and energy efficiency of the system.—Previous sections have shown that the influences of varying R_{wsp}, R_m, and R_p on the current deviation and the extractable energy content of the system is negligible for a 1 C constant-current discharge. Therefore, the influence of various C-rates is investigated to demonstrate both the rate capability and the influence of varying contact resistances on the extractable energy content of the system. For this purpose, various C-rates (1, 1.25, 1.5, 1.75, 2, 2.25, 2.5, 2.75, and 3) were applied to a 4s4p system connected on the left (ST-left). Additionally, a variation of $R_{p,2}$ by +100% was accomplished to examine whether the extractable energy content differs significantly from the homogeneous case. As it is assumed that the analysis of the extractable energy content is more meaningful for the rate capability of the system than the maximum current deviation at a specific point in time, the following analysis focuses on the extractable energy content. Since the previous sections have shown that the variations of R_{wsp} and R_m have a minor influence compared to R_p, an additional analysis of the variation of R_{wsp} and R_m is omitted here. Furthermore, an additional analysis of ST-cross was not conducted due to the symmetry effects shown in Fig. 5.

Figure 10 illustrates the extractable energy content for the homogenous case (solid line) and for a variation of $R_{p,2}$ (dashed line) for the C-rates named above. Comparing the homogeneous and

varied cases, significant deviation of the extractable energy content cannot be depicted, since the maximum deviation calculates to 0.03%. Furthermore, the rate capability of the extractable energy content can be divided into two branches. The first one is represented by the range of 1 C to 1.75 C. In this domain, the extractable energy content decreases from 99.1% (1 C) to 94.5% (1.75 C) for both cases, which equals a mean decrease of 1.53% per increase of C-rate by 0.25 C. Within the second branch, the mean gradient of energy content per increase of the C-rate by 0.25 increases to 7.54% in the remaining range between 1.75 C and 3 C. This results in an extractable energy content of 56.8% for an applied 3 C-rate.

Consequently, the analysis clearly shows the trend of a decreasing rate capability of the extractable energy content with increasing C-rates. Furthermore, the findings show that an increased contact resistance leads to a more uneven current distribution, but that the extractable energy content remains the same. This leads to the assumption that the almost constant energy output is achieved by higher loads on individual system components, which is why the longevity has to be investigated further. In addition, for future studies the cell parametrization can be further specified in subsequent steps, as shown by Mao et al.[31] and Rheinfeld et al.[32] These extensions would take into account additional limitations of electrode kinetics, and thus increase the accuracy of the p2D model in the event of even higher C-rates, especially higher than 3 C. Table V summarizes the results of the investigated cases.

Conclusions

In this study, the structure of the ELM which describes battery cells connected in serial and in parallel as described in Ref. 13 is extended to include flexible STs and cross-connectors. Based on this extension, the influence of ST-left and ST-cross, as well as the influence of the welding seam resistance, the cross-connector resistance and the string connector resistance on the current distribution within a 4s4p system including cross connectors are examined. Finally, the rate capability and the energy efficiency of the systems are investigated for different C-rates.

If cross-connectors are implemented in the system, the choice of the ST is negligible. Moreover, depending on the choice of the ST, symmetries can be found within the analyzed system. Thus, ST-side leads to axis symmetry to the middle axis of the system, whereas ST-cross leads to point symmetry to the system's center point. For the homogeneous case, the maximum current deviations within the analyzed system could be found at the BoD and at the EoD with a maximum deviation of 1.9% and 2.4%, respectively. With increasing distance to the ST, the current deviation decreases at the BoD, but increases at the EoD. These deviations occur in cell packages I and IV, whereas the deviation within cell packages II and III is nearly zero and therefore negligible.

Furthermore, an increased welding seam resistance by 100% alters the current distribution of all cells in the respective cell package, but does not affect other cell packages within the system. This is due to the presence of cross-connectors, which is why cross-connectors can be seen as balancing elements. Additionally, an increase of a cross-connector resistance by 100% has no significant influence on the current distribution within the system. If the maximum deviations of the cell packages are compared with one

Table V. Summary of the investigated cases.

Investigation	Initial Value	Variation	Critical Component	Result
ST	—	left, cross	cross-connectors	both $\Delta I_{max} = +2.40\%$ axis and point symmetry
R_{wsp}	62.5 $\mu\Omega$	+100%	$R_{wsp,1,4}$	$\Delta I_{max} = +5.50\%$
R_m	15.4 $\mu\Omega$	+100%	$R_{m,1,2}$	$\Delta I_{max} = +0.02\%$
R_p	15.4 $\mu\Omega$	+100%	$R_{p,2}$	$\Delta I_{max} = +3.20\%$
i_{app}	1 C per cell	C-rate		$\Delta E_{max} = -43.2\%$ (3 C)

another, a variation of a welding seam resistance on one of the enclosed cell packages II and III shows the greatest influence.

Moreover, the variation of the string connector resistances by 100% showed that the influence of the string connectors on the current distribution dominates the influence of the welding seam resistance. Thus, particular attention should be paid to the assembling process. Additionally, the investigation showed that string connectors can be seen as segmenting elements of the system.

The extractable energy content of the investigated system remained almost the same for all examined cases performed with a constant current discharge of 1 C. This in turn means that the measurable energy content cannot be used as an indicator for inhomogeneous welding seam resistances, cross-connector resistances, or string connector resistances within the system.

Finally, the investigation of the rate capability of the system showed that the extractable energy content decreases non-linearly with the C-rate. Furthermore, the extractable energy content under a variation of a string connector resistance remained almost the same as compared to the homogeneous case. This in turn means that the nearly constant output is achieved by higher load on individual system components, and thus the long-term durability has to be investigated further.

Future studies should therefore verify these results using measurement data. In particular, the heat input into the cells resulting from increased resistances as well as temperature gradients in general should be analyzed. Further extensions of the model could take into account additional limitations of electrode kinetics to improve the model's high current behavior. Furthermore, the influence of inhomogeneous current distribution on the aging behavior of parallel-connected cells should also be investigated.

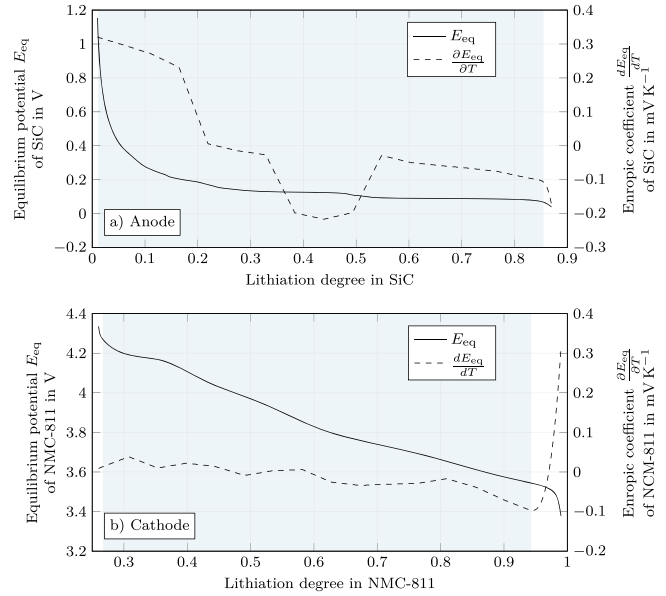## Appendix. Model Characteristics

Figure A·1. Characteristics of the investigated cell. (a) and (b) illustrate the E_{eq} and entropic coefficient $\frac{\partial E_{eq}}{\partial T}$ of anode and cathode. The highlighted areas correspond to the usable voltage window.

Table A·I. Equations for the single p2D model.

	Electrochemical-thermal model (single p2D)
Mass balance [I]	$\varepsilon_l \frac{\partial c_l(x,t)}{\partial t} = \frac{\partial}{\partial x}\left(D_l^{\text{eff}} \frac{\partial c_l(x,t)}{\partial x} + \frac{i_l(x,t)(1-t_+^0)}{F}\right)$
	$\varepsilon_s \frac{\partial c_s(x,t,r)}{\partial t} = \frac{1}{r^2}\frac{\partial}{\partial r}\left(D_s r^2 \frac{\partial c_s(x,t,r)}{\partial r}\right)$
Potentials [I]	$\frac{\partial \Phi_l(x,t)}{\partial x} = -\frac{i_l(x,t)}{\kappa_l^{\text{eff}}} + \frac{2RT}{F}(1-t_+^0)\left(1 + \frac{d\ln f_\pm}{d\ln c_l(x,t)}\right)\frac{\partial \ln c_l(x,t)}{\partial x}$
	$\frac{\partial \Phi_s(x,t)}{\partial x} = -\frac{i_{c_i}(t)-i_l(x,t)}{\sigma_s}$ with $i_{c_i}(t) = i_s(x,t) + i_l(x,t)$ $\forall x, t$
Charge balance [I]	$\frac{\partial i_l(x,t)}{\partial x} + \frac{\partial i_s(x,t)}{\partial x} = 0$ with $\frac{\partial i_s(x,t)}{\partial x} = -\frac{3\varepsilon_s}{r_p}Fj_n(x,t)$
Electrode Kinetics [I]	$j_n(x,t) = \frac{i_0(x,t)}{F}\left[\exp\left(\frac{\alpha_a F \eta(x,t)}{RT}\right) - \exp\left(-\frac{\alpha_c F \eta(x,t)}{RT}\right)\right]$
	$\eta(x,t) = \Phi_s(x,t) - \Phi_l(x,t) - E_{eq}(x,t) - j_n(x,t)FR_f$
	$i_0(x,t) = F\,k\,(c_{s,\max} - c_{ss}(x,t))^{\alpha_c}\,(c_{ss}(x,t))^{\alpha_a}(c_l(x,t))^{\alpha_a}$
Temperature [I,II]	$m\,c_p \frac{\partial T}{\partial t} = A \cdot q_{\text{p2D}} + Q_{\text{IH}} - Q_{\text{conv}} - Q_{\text{rad}}$
Heat sources	$q_r = \frac{3\varepsilon_s F}{r_p}\int_{x*} j_n \cdot \eta\;dx$
	$q_{\text{rev}} = \frac{3\varepsilon_s F}{r_p}\int_{x*} j_n \cdot \frac{\partial E_{eq}}{\partial T} \cdot T\;dx$
	$q_l = \int_{x=0}^{L_{\text{neg}}+L_{\text{sep}}+L_{\text{pos}}} i_l \cdot \frac{\partial \Phi_l}{\partial x}\;dx$
	$q_s = \int_{x*} i_s \cdot \frac{\partial \Phi_s}{\partial x}\;dx$
	$q_{\text{p2D}} = q_r + q_{\text{rev}} + q_l + q_s$
	$Q_{\text{IH}} = i_{c_i}^2 \cdot R_{\text{IH}}$
	$Q_{\text{conv}} = \alpha_{\text{conv}} A_{\text{surf}}(T - T_\infty)$
	$Q_{\text{rad}} = \varepsilon_{\text{rad}}\,\sigma_B\,A_{\text{surf}}(T^4 - T_\infty^4)$

[I] Ref. 33 [II] Ref. 34 $x* = x \in [0, L_{\text{neg}}] \wedge [L_{\text{neg}} + L_{\text{sep}}, L_{\text{neg}} + L_{\text{sep}} + L_{\text{pos}}]$.

Table A·II. Parameterization of the single p2D model with NMC-811/SiC electrodes.

Geometry	Silicon-graphite (SiC)	Separator	Nickel-rich NMC-811
Thickness L	86.7 μm [m]	12 μm [m]	66.2 μm [m]
Particle radius r_p	6.1 μm [m,D50]		3.8 μm [m,D50]
Active material fraction ε_s	69.4% [e]		74.5% [e]
Inactive fraction $\varepsilon_{s,na}$	9% [e,*]		8.4% [e,*]
Porosity ε_l	21.6% [m]	45% [e]	17.1% [m]
Bruggeman coefficient β [V II,**]	1.5	1.5	1.85 [e]
Thermodynamics			
Equilibrium potential E_{eq}	see Fig. A·1a [m]		see Fig. A·1b [m]
Entropic coefficient $\frac{\partial E_{eq}}{\partial T}$	see Fig. A·1a [m]		see Fig. A·1b [m]
Stoichiometry 100% SoC	0.852		0.222
0% SoC	0.002		0.942
Max. theoretical loading b_g	415 mAh g^{-1} [I]		275.5 mAh g^{-1} [II]
Density ρ	2.24 g cm^{-3} [I]		4.87 g cm^{-3} [II]
Concentration $c_{s,max}$	34684 mol m^{-3} [e]		50060 mol m^{-3} [e]
Transport			
Solid diffusivity D_s ***	5 · 10^{-14} m^2 s^{-1} [e,V]		5 · 10^{-13} m^2 s^{-1} [IV,VI]
Specific activation $\frac{E_{a,D_s}}{R}$ ***	1200 K [e]		1200 K [e]
Solid conductivity σ_s	100 S m^{-1} [IV]		0.17 S m^{-1} [e,IV]
Film resistance R_f	0.0035 Ω m^2 [III]		0 Ω m^2 [e]
Kinetics			
Reaction rate constant k ***	3 · 10^{-11} m s^{-1} [e]		1 · 10^{-11} m s^{-1} [e]
Specific activation $\frac{E_{a,k}}{R}$ ***	3600 K [e]		3600 K [e]
Transfer coefficient $\alpha_{a/c}$	0.5 [e]		0.5 [e]

m = measured e = estimated * PVDF binder/Carbon black (Refs. 35, 36).
[I] Ref. 37. [II] Ref. 38 [III] Ref. 31 [IV] Ref. 39 [V] Ref. 40 [VI] Ref. 41 [VII] Ref. 42.
** Effective transport correction according to Bruggeman (Ref. 42): $\Psi_{eff} = \varepsilon^\beta \cdot \Psi_0$.
*** Arrhenius law (Ref. 43): $i(T) = i \cdot \exp\left(\frac{E_{a,i}}{R} \frac{(T - 298[K])}{T \cdot 298[K]}\right)$ with $i \in k \wedge D_s$.

Table A·III. Nomenclature

Greek symbols

Symbol	Unit	Description
α		Transfer coefficient
α_{conv}	W m^{-2} K^{-1}	Heat transfer coefficient
β		Bruggeman coefficient
ε		Volume fraction
ε_{rad}		Radiation emission coefficient
η	V	Overpotential
κ	S m^{-1}	Ionic conductivity
ρ	kg m^{-3}	Mass density
σ	S m^{-1}	Electrical conductivity
σ_B	5.67 · 10^{-8} W m^{-2} K^{-4}	Stefan-Boltzmann constant
ϕ	V	External cell potential between cell terminals
Φ	V	Internal electrical potential

Latin symbols

Symbol	Unit	Description
a	m^{-1}	Specific surface
A	m^2	Surface area
A		Anode (domain)
c	mol m^{-3}	Concentration of lithium cations (Li$^+$)
$c_{s,max}$	mol m^{-3}	Maximum theoretical concentration of Li$^+$
c_i		Cell under consideration
c_p	J kg^{-1} K^{-1}	Heat capacity
C		Cathode (domain)
D	m^2 s^{-1}	Diffusion coefficient
E_{eq}	V	Equilibrium potential vs Li/Li$^+$
E_{hom}	Wh	Extractable system energy content for the homogeneous case

Table A·III. (Continued).

Latin symbols

$E_{N,cell}$	Wh	Nominal cell energy content
$E_{N,sys}$	Wh	Nominal system energy content
E_{sys}	Wh	Extractable system energy content
$f_{\pm}$		Mean molar activity coefficient of electrolyte
F	$96\,485$ A s mol^{-1}	Faraday's constant
i	A m^{-2}	Current density
I_i	A	Current through single cell
I_{app}	A	Current applied to the system
I_{1C}	A	Current applied to the cell equals 1 C
I_{3C}	A	Current applied to the cell equals 3 C
I_m	A	Current through cross-connector
i_0	A m^{-2}	Exchange current density
j_n	mol m^{-2} s^{-1}	Pore-wall flux
k	m s^{-1}	Reaction rate constant
k_i		Current node (Kirchhoff)
l_{ws}	m	Length of welding seam
L	m	Thickness
m	kg	Mass of the jelly roll
m_i		Mesh (Kirchhoff)
N_{GCP}		Number of group current paths
r	m	Radial coordinate in active particles of p2D model
r_p	m	Particle radius
R	8.314 J mol^{-1} K^{-1}	Gas constant
R_{IH}	Ωm^2	Internal heat resistance
R_P	m	Particle radius
R_{conn}	Ω	Resistance of the serial connection within a string
R_f	Ω	Film resistance
R_i	Ω	Internal Resistance
R_m	Ω	Cross-connector resistance
R_n	Ω	String connector resistance (negative tab)
R_p	Ω	String connector resistance (positive tab)
R_{PR}	Ω	Path resistance
R_{wsn}	Ω	Welding seam resistance (negative tab)
R_{wsp}	Ω	Welding seam resistance (positive tab)
S		Separator (domain)
ST		System terminal
SF		Scaling factor
q	W m^{-2}	Heat generation rate per area
Q	W	Heat generation rate
Q_{IH}	W	Internal heat
t	s	Time
T	K	Temperature
t_0^+		Transport number of Li$^+$
x		x-coordinate in p2D model
X		Number of cells connected in serial
Y		Number of cells connected in parallel

Indices

Symbol		Description
a		Anodic reaction (oxidation)
c		Cathodic reaction (reduction)
conv		Heat convection
eff		Transport corrected (Bruggeman correlation)
l		Liquid phase (i.e. electrolyte)
neg		Negative electrode
pos		Positive electrode
rad		Heat radiation
r		Reaction heat
rev		Reversible heat
s		Solid phase (i.e. active particle)
sep		Separator
ss		Active particle surface in solid phase
surf		Surface

ORCID

Markus Schindler https://orcid.org/0000-0002-3784-6339
Axel Durdel https://orcid.org/0000-0002-0479-5491
Johannes Sturm https://orcid.org/0000-0001-8876-9989
Philipp Jocher https://orcid.org/0000-0003-1335-8434
Andreas Jossen https://orcid.org/0000-0003-0964-1405

References

1. L. Noel, G. Zarazua de Rubens, B. K. Sovacool, and J. Kester, "Fear and loathing of electric vehicles: the reactionary rhetoric of range anxiety." *Energy Research & Social Science*, **48**, 96 (2019).
2. M. J. Brand, M. H. Hofmann, M. Steinhardt, S. F. Schuster, and A. Jossen, "Current distribution within parallel-connected battery cells." *Journal of Power Sources*, **334**, 202 (2016).
3. M. H. Hofmann, K. Czyrka, M. J. Brand, M. Steinhardt, A. Noel, F. B. Spingler, and A. Jossen, "Dynamics of current distribution within battery cells connected in parallel." *Journal of Energy Storage*, **20**, 120 (2018).
4. Y. Merla, B. Wu, V. Yufit, R. F. Martinez-Botas, and G. J. Offer, "An easy-to-parameterise physics-informed battery model and its application towards lithium-ion battery cell design, diagnosis, and degradation." *Journal of Power Sources*, **384**, 66 (2018).
5. R. E. Gerver and J. P. Meyers, "Three-dimensional modeling of electrochemical performance and heat generation of lithium-ion batteries in tabbed planar configurations." *J. Electrochem. Soc.*, **158**, A835 (2011).
6. K. Rumpf, M. Naumann, and A. Jossen, "Experimental investigation of parametric cell-to-cell variation and correlation based on 1100 commercial lithium-ion cells." *Journal of Energy Storage*, **14**, 224 (2017).
7. F. An, J. Huang, C. Wang, Z. Li, J. Zhang, S. Wang, and P. Li, "Cell sorting for parallel lithium-ion battery systems: evaluation based on an electric circuit model." *Journal of Energy Storage*, **6**, 195 (2016).
8. M.-S. Wu, C.-Y. Lin, Y.-Y. Wang, C.-C. Wan, and C. R. Yang, "Numerical simulation for the discharge behaviors of batteries in series and/or parallel-connected battery pack." *Electrochimica Acta*, **52**, 1349 (2006).
9. M. Baumann, L. Wildfeuer, S. Rohr, and M. Lienkamp, "Parameter variations within Li-Ion battery packs—theoretical investigations and experimental quantification." *Journal of Energy Storage*, **18**, 295 (2018).
10. S. Miyatake, Y. Susuki, T. Hikihara, S. Itoh, and K. Tanaka, "Discharge characteristics of multicell lithium-ion battery with nonuniform cells." *Journal of Power Sources*, **241**, 736 (2013).
11. B. Wu, V. Yufit, M. Marinescu, G. J. Offer, R. F. Martinez-Botas, and N. P. Brandon, "Coupled thermal-electrochemical modelling of uneven heat generation in lithium-ion battery packs." *Journal of Power Sources*, **243**, 544 (2013).
12. A. Fill, S. Koch, A. Pott, and K.-P. Birke, "Current distribution of parallel-connected cells in dependence of cell resistance, capacity and number of parallel cells." *Journal of Power Sources*, **407**, 147 (2018).
13. K. Rumpf, A. Rheinfeld, M. Schindler, J. Keil, T. Schua, and A. Jossen, "Influence of cell-to-cell variations on the inhomogeneity of lithium-ion battery modules." *J. Electrochem. Soc.*, **165**, A2587 11 (2018).
14. N. Yang, X. Zhang, B. Shang, and G. Li, "Unbalanced discharging and aging due to temperature differences among the cells in a lithium-ion battery pack with parallel combination." *Journal of Power Sources*, **306**, 733 (2016).
15. S. Kamalisiahroudi, J. Huang, L. Zhe, and J. Zhang, "Study of temperature difference and current distribution in parallel-connected cells at low temperature." *International Journal of Mechanical and Mechatronics Engineering*, **8**, 1596 (2014).
16. M. Guo and R. E. White, "Thermal model for lithium ion battery pack with mixed parallel and series configuration." *J. Electrochem. Soc.*, **158**, A1166 (2011).
17. Y. Zhang, J. Zheng, S. Lin, F. Bai, W. H. Tanveer, S. Cha, X. Wu, and W. Feng, "Nonuniform current distribution within parallel-connected batteries." *International Journal of Energy Research*, **42**, 2835 (2018).
18. L. Wang, Y. Cheng, and X. Zhao, "Influence of connecting plate resistance upon LiFePO₄ battery performance." *Applied Energy*, **147**, 353 (2015).
19. T. Grün, K. Stella, and O. Wollersheim, "Influence of circuit design on load distribution and performance of parallel-connected Lithium ion cells for photovoltaic home storage systems." *Journal of Energy Storage*, **17**, 367 (2018).
20. N. Ganesan, S. Basu, K. S. Hariharan, S. M. Kolake, T. Song, T. Yeo, D. K. Sohn, and S. Doo, "Physics based modeling of a series parallel battery pack for asymmetry analysis, predictive control and life extension." *Journal of Power Sources*, **322**, 57 (2016).
21. R. Spurrett, C. Thwaite, A. Holland, D. Lizius, and G. Dudley, "Modeling of highly-parallel lithium-ion batteries." *EDS*, **6**, 685 (2002).
22. N. Damay, C. Forgez, G. Friedrich, and M.-P. Bichat, "Heterogeneous behavior modeling of a LiFePO₄-graphite cell using an equivalent electrical circuit." *Journal of Energy Storage*, **12**, 167 (2017).
23. J. Sturm, A. Rheinfeld, I. Zilberman, F. B. Spingler, S. Kosch, F. Frie, and A. Jossen, "Modeling and simulation of inhomogeneities in a 18 650 nickel-rich, silicon-graphite lithium-ion cell during fast charging." *Journal of Power Sources*, **412**, 204 (2019).
24. J. Sturm, S. Ludwig, J. Zwirner, C. Ramirez-Garcia, B. Heinrich, M. F. Horsche, and A. Jossen, "Suitability of physicochemical models for embedded systems regarding a nickel-rich, silicon-graphite lithium-ion battery." *Journal of Power Sources*, **436**, 226834 (2019).
25. LG Chem, Automotive Battery (2019), www.lgchem.com.
26. AUDI AG Communication, Audi e-tron - Battery and Safety (2018), https://audi-technology-portal.de/en.
27. Jaguar Land Rover Limited, JAGUAR I-PACE: THE ART OF ELECTRIC PERFORMANCE (2018), https://media.jaguar.com/2018/jaguar-i-pace-art-electric-performance.
28. M. Wienkötter, The Battery: Sophisticated Thermal Management, 800-volt System Voltage (2019), https://newsroom.porsche.com/en/products/taycan/battery-18557.html.
29. P. A. Schmidt, P. Schmitz, and M. F. Zaeh, "Laser beam welding of electrical contacts for the application in stationary energy storage devices." *Journal of Laser Applications*, **28**, 022423 (2016).
30. A. Nyman, T. G. Zavalis, R. Elger, M. Behm, and G. Lindbergh, "A new methodology for evaluating the high-power behavior of a li-ion battery cell." *ECS Transactions*, **25**(36), 253 (2010).
31. J. Mao, W. Tiedemann, and J. Newman, "Simulation of temperature rise in Li-ion cells at very high currents." *Journal of Power Sources*, **271**, 444 (2014).
32. A. Rheinfeld, J. Sturm, A. Noel, J. Wilhelm, A. Kriston, A. Pfrang, and A. Jossen, "Quasi-isothermal external short circuit tests applied to lithium-ion cells: part ii. modeling and simulation." *J. Electrochem. Soc.*, **166**, A151 (2019).
33. M. Doyle, "Modeling of galvanostatic charge and discharge of the lithium/polymer/insertion cell." *J. Electrochem. Soc.*, **140**, 1526 (1993).
34. D. Bernardi, "A general energy balance for battery systems." *J. Electrochem. Soc.*, **132**, 5 (1985).
35. C. M. Long, M. A. Nascarella, and P. A. Valberg, "Carbon black vs black carbon and other airborne materials containing elemental carbon: Physical and chemical distinctions." *Environmental Pollution (Barking, Essex : 1987)*, **181**, 271 (2013).
36. G. Liu, H. Zheng, A. S. Simens, A. M. Minor, X. Song, and V. S. Battaglia, "Optimization of acetylene black conductive additive and pvdf composition for high-power rechargeable lithium-ion cells." *J. Electrochem. Soc.*, **154**, A1129 (2007).
37. R. Dash and S. Pannala, "Theoretical limits of energy density in silicon-carbon composite anode based lithium ion batteries." *Sci. Rep.*, 274496 (2016).
38. R. Jung, M. Metzger, F. Maglia, C. Stinner, and H. A. Gasteiger, "Oxygen release and its effect on the cycling stability of LiNiₓMnᵧCoᵤO₂ (NMC) cathode materials for li-ion batteries." *J. Electrochem. Soc.*, **164**, A1361 (2017).
39. H.-J. Noh, S. Youn, C. S. Yoon, and Y.-K. Sun, "Comparison of the structural and electrochemical properties of layered Li[NiₓMnᵧCoᵤ]O₂ (x = 1/3, 0.5, 0.6, 0.7, 0.8 and 0.85) cathode material for lithium-ion batteries." *Journal of Power Sources*, **233**, 121 (2013).
40. M. Doyle and Y. Fuentes, "Computer simulations of a lithium-ion polymer battery and implications for higher capacity next-generation battery designs." *J. Electrochem. Soc.*, **150**, A706 (2003).
41. D. Andre, S.-J. Kim, P. Lamp, S. F. Lux, F. Maglia, O. Paschos, and B. Stiaszny, "Future generations of cathode materials: an automotive industry perspective." *Journal of Materials Chemistry A*, **3**, 6709 (2015).
42. D. A. G. Bruggeman, "Calculation of different physical constants in heterogenous substances." *Ann. Phys.*, **416**, 636 (1935).
43. S. Arrhenius, "About the inversion rate of sucrose caused by acids." *Z. Phys. Chem.*, **4**U, 226 (1889).